# High resolution observations of 6.7-GHz methanol masers with the LBA

R. Dodson[1,3], R. Ojha[2], S. P. Ellingsen[3]★

[1] *ISAS, 3-1-1 Yoshinodai, Sagamihara, Japan*

[2] *ATNF, CSIRO, PO 76, Epping 1710, Australia*

[3] *School of Mathematics and Physics, University of Tasmania, Private bag 37, Hobart, Tasmania 7000, Australia*

2 February 2008

**ABSTRACT**

We have used the Australian Long Baseline Array (LBA) to produce milliarc-second images of five sites of methanol ($CH_3OH$) maser emission at 6.7 GHz. These are all sites that have linear morphologies at arcsecond resolutions, which have been hypothesised to be due to the masers forming in edge-on circumstellar disks. We find that a simple disk model cannot explain the observations. We discuss various alternatives, and suggest a new model which explains how linear velocity gradients can be produced in methanol masers that arise in planar shocks propagating nearly perpendicular to the line of sight.

**Key words:** molecules — masers — radio lines : $CH_3OH$ G327.12+0.5, G327.40+0.4, G328.24-0.5, G328.81+0.6, G329.03-0.2

## 1 INTRODUCTION

Massive stars play a crucial role in the evolution of galaxies. They are the cauldrons where heavy elements are produced. They provide turbulent energy to the interstellar medium, are involved in the production and destruction of molecular clouds and may regulate the rate of star formation. Despite their importance, the processes leading to massive star formation are poorly understood (e.g. Garay & Lizano (1999), McKee & Tan (2003)). Apart from theo-

★ E-mail:rdodson@vsop.isas.jaxa.jp; rojha@atnf.csiro.au; Simon.Ellingsen@utas.edu.au

retical complexities inherent in such a multiple-process problem (Yorke & Sonnhalter 2002), the chief obstacle to our understanding is observational – massive star formation occurs in fewer regions (as they form quickly) that are, on average, further away (than regions of low-mass star formation) and are highly obscured at optical wavelengths (Churchwell et al. (1990), Plume et al. (1992)).

Interstellar masers of three molecules, $H_2O$, OH and methanol, are both powerful and widely associated with active high-mass star formation regions (Forster & Caswell (1989), Menten (1991)). Thus, they have long been recognized as a potentially powerful tool to study the physical conditions and kinematics of massive star formation sites. However, the complex distribution of $H_2O$ and OH masers has limited their role in the elucidation of massive star formation. Further, both $H_2O$ and OH masers are also found towards other objects such as evolved low-mass stars (Wilson & Barrett 1972) and the centres of galaxies (Dos Santos & Lepine 1979).

The two strongest class II methanol masers (i.e. those closely associated with OH masers and strong far-infrared emission) were discovered at 12.178593 GHz by Batrla et al. (1987) and at 6.668518 GHz by Menten (1991). These methanol masers are closely associated with high-mass star forming regions (Norris et al. 1988; Walsh et al. 1997). Sensitive searches for 6.7-GHz methanol masers towards low-mass star forming regions (Minier et al. 2003), and nearby active galaxies (Phillips et al. 1998; Darling et al. 2003) have failed to detect any. While untargeted searches covering large areas of the Galactic Plane have detected many new 6.7-GHz methanol masers not associated with known massive star forming regions, to date none have been confirmed as being associated with any other type of astrophysical object (Caswell 1996; Ellingsen et al. 1996; Szymczak et al. 2002). Thus class II methanol masers prove more efficacious for finding and studying high-mass star forming regions than either $H_2O$ or OH masers.

The brightness of methanol masers allows high resolution interferometric observations to be made, which provide accurate measurements of position, velocity and dimensions of the individual maser components. Previous interferometric observations have generally used connected element interferometers (Norris et al. 1988, 1993; Phillips et al. 1998; Walsh et al. 1998) that offer resolutions of the order of arcseconds (which can be improved upon by super resolving the velocity features, see Phillips et al. (1998), hereafter P98), though some VLBI (Very Long Baseline Interferometry) experiments (Menten et al. 1988, 1992; Norris et al. 1998; Minier et al. 1998; Moscadelli et al. 1999) with milliarcsecond resolution have been

performed. VLBI resolution images are vital to uncovering the structure of these masing regions and their paucity comes from the absence of telescopes (let alone arrays of telescopes) able to observe at these frequencies until relatively recently. This situation has now changed with both the Australian Long Baseline Array (LBA[1], Ojha (2004)) and the European VLBI Network (EVN) covering the 6.7-GHz transition, while the LBA and the Very Long Baseline Array (VLBA) covers the 12.2-GHz transition.

Many of the observed masing sites have individual masers located along lines or arcs, often with a near-monotonic velocity gradient along the line. It has been suggested (Norris et al. 1993, 1998; Phillips et al. 1998) that these linear structures trace masers embedded in an edge-on disk surrounding a young star. Values of disk radii and enclosed masses derived from modelling these sources assuming Keplerian rotation, agree with theoretical models of accretion disks around massive stars (Lin & Pringle 1990; Hollenbach et al. 1994).

Walsh et al. (1998) found 36 of 97 maser sites to be linearly extended and, while the circumstellar disk hypothesis is consistent with their data, they considered it unlikely as the derived values of the enclosed mass are too high in some cases. They suggested the linear geometry of 6.7-GHz methanol masers resulted from shocks arising behind a smooth shock front. As shocks would not produce the velocity gradient they saw in many of their maser sites, Norris et al. (1993) had rejected shocks as a possible explanation. Pointing out that most maser sites in their larger sample do not show a systematic velocity gradient, Walsh et al. (1998) argue that a velocity gradient is not typical in maser sites. The VLBI observations of Minier et al. (2000) find the linear extent of maser regions to be about 10 times smaller than that seen at lower resolutions. This yields sub-solar masses for the "massive" star. Both edge-on shock and edge-on disk models produce linear features across the sky but shock fronts are not normally so well ordered. At milliarcsecond (mas) resolutions we probe resolutions of the order of tens of AU, the perfect scale to investigate these differences.

The case for disks, or the other models, will only become clearer after a significant increase in the sample size of methanol masers imaged at very high resolution. We present the first VLBI images of five sources which have not previously been imaged at mas resolution. This allows us to directly compare conclusions based on the ATCA (Australia Telescope Compact Array) data to those reached with more than two orders of magnitude better resolution.

---

[1] The Long Baseline Array is part of the Australia Telescope which is funded by the Commonwealth of Australia for operation as a National Facility managed by CSIRO.

**Table 1.** Observed Maser Sites. Absolute positions for the strongest features are from (1) Phillips et al.(1998) (2) Caswell (1997) and (3) Caswell et al.(1995). Relative positions are with respect to these absolute positions. Diameters, where calculated, are based on the nearer kinematic distances and the enclosed masses were calculated from a linear least-squares fit in a velocity-major axis diagram under the assumption that the masers arise in an edge-on disk.

| Source | Right Ascension (J2000) | Declination (J2000) | Mean LSR Velocity (km s$^{-1}$) | Distance (kpc) | Peak zero *uv* Flux Density (Jy) | Diameter (AU) | Mass M$_\odot$ | Position Reference |
|---|---|---|---|---|---|---|---|---|
| G327.120+0.511 | 15:47:32.71 | −53:52:38.5 | −87.3 | 5.5/8.8 | 27.5 | 1900 | 17 | 1 |
| G327.402+0.444 | 15:49:19.50 | −53:45:13.9 | −81.8 | 5.1/9.2 | 233 | 239 | 0.9 | 1 |
| G327.402+0.444E | 15:49:19.72 | −53:45:14.6 | | | 1.5 | - | - | |
| G327.402+0.445 | 15:49:19.33 | −53:45:14.4 | | | 18 | 1392 | 9.2 | |
| G328.237−0.548 | 15:57:58.27 | −53:59:23.1 | −43.8 | 3.0 | 195 | 463 | 0.4 | 1 |
| G328.237−0.548W | 15:57:58.20 | −53:59:23.2 | | | 5.5 | 560 | 2.5 | |
| G328.254−0.532 | 15:57:59.73 | −53:58:00.8 | −37.5 | 2.6 | 47 | 141 | 0.0 | |
| G328.808+0.633 | 15:55:48.50 | −52:43:06.64 | −45.1 | 3.1 | 148 | 1713 | 0.4 | 2 |
| G328.809+0.633 | 15:55:48.62 | −52:43:06.55 | | | 29.9 | - | - | |
| G329.029−0.205 | 16:00:31.80 | −53:12:49.7 | −37.3 | 2.6 | 114 | 164 | 1.0 | 3 |
| G329.031−0.198 | 16:00:30.33 | −53:12:27.4 | −45.6 | 3.1 | 5.7 | 612 | 4.2 | |

In Section §2 we describe our observations and the data reduction path. Our results are presented in §3 and their implications for the current models are discussed in §4. §5 sets out our conclusions.

## 2   OBSERVATIONS AND DATA REDUCTION

### 2.1   Observations

The LBA is equipped to observe at 6.7 GHz at five of its antennas: Parkes, ATCA, Mopra, Hobart and Ceduna. Thus, at this frequency, this array provides baselines up to ∼ 1700 km, yielding a resolution of 5.3 mas.

The LBA uses the S2 recording system (Cannon et al. 1997; Wilson et al. 1995). We used a bandwidth of 4-MHz centred on 6670 MHz. The LBA correlator formed 1024 channels across this bandwidth, a velocity resolution of 0.2 km s$^{-1}$ per channel. Both circular polarizations were recorded, but only the parallel hand products were formed as we had not included polarisation calibrators in the schedule.

These observations were made on December 21$^{st}$ and 22$^{nd}$ 1999 for a total of 10.5 hours. Each target was typically observed for a total of 1.8 hours with six 'cuts' on the source. We observed a calibrator source on average every eighty minutes in order to determine the delays and bandpasses.

## 2.2   Methods

Post correlation we loaded the visibilities into NRAO's Astronomical Image Processing System (AIPS, Greisen (1988)), where we followed the conventional path for spectral line VLBI calibration (Diamond 1989). Delays and rates were determined from the calibrator scans, and the rates only were calculated for the target sources. The velocities were corrected to the local standard of rest using the AIPS task CVEL. The autocorrelation peak velocity was corrected to match those found in the position references. Amplitude calibration was achieved through scaling the maser autocorrelations, which were output from the correlator at the same time as the cross products. Once gain calibration was complete we exported the data for final selfcalibration in the Caltech package DIFMAP (Shepherd 1997). The relative positions shown in the figures are with respect to the absolute positions given in Table 1.

Model fitting was performed on each channel independently by selecting the minimum number of model parameters with a peak flux density greater than five times the residual RMS (which is about 10 mJy/beam in line free channels). All those model fits which were weak and isolated in frequency and position were rejected. Care was taken to search for all components within the field of view (2.5′). We discovered several maser emission clusters which had not been detected previously as they merged with stronger emission at the same velocity in the lower resolution ATCA observations.

The models fitted by DIFMAP were processed with MSPLOT which was written by C. Phillips[2] for just this kind of analysis. Error estimates were based on the synthesised beam size over the signal to noise (defined as the flux per beam over residual image RMS). By model-fitting we can also calculate the equivalent flux density at zero *uv* spacing, which can be directly compared with the autocorrelation spectrum.

For those sources that were near to the phase centre and therefore well imaged, there is no significant difference between the equivalent zero spacing flux density and the flux density observed in the autocorrelation spectra (taken from a subset of the Parkes observations). We can therefore be confident that we have not missed any significant maser emission in these regions and there is no need to assume the existence of halos as in some other sources (Minier et al. 2002).

If we assume that the methanol maser emission is coming from an edge-on disk we can calculate the contained mass from the velocity gradient along the major axis, and there-

---

[2] http://www.atnf.csiro.au/people/Chris.Phillips/software.html

fore an upper limit on the mass of the central star (Norris et al. 1998; Walsh et al. 1998). The fact that these parameters derived from the ATCA observations agreed well with the predicted masses and dimensions (tens of $M_\odot$ and thousands of AU, Lin & Pringle (1990)) provided compelling support for the disk model. We have used the kinematic distance model of Clemens (1985) to estimate the distances of the masers based upon their flux-density weighted mean velocity averaged across the arcsecond scale cluster. This reduces the effect of the internal motions within the larger star forming region.

## 3   RESULTS

We observed five 6.7-GHz methanol maser sites, and detected eleven clusters of emission within these sites. These clusters, their positions and the mass of the central star calculated from the methanol maser velocity gradient are listed in Table 1.

In the figures we plot the maser emission sites and clusters relative to the position reference, with the spots sizes proportional to the flux density, and 1-$\sigma$ error bars. In the plots of the spatial distribution of the maser emission the colour of the points represent the velocity of the emission and the origin of the axes corresponds to the position given in Table 1. For most masers the error in the relative position is smaller than the size of the points and so the error bars are not visible. The line of best fit to the maser emission is used to determine the major axis of the cluster.

For those sites of maser emission for which we determined the major axis we have also produced plots of the maser velocity versus the offset along the major axis. In these plots the colour of each point represents it's distance (in mas) from the line of best fit in the corresponding spatial plots (i.e. its offset in the minor axis direction). The line of best fit to the velocity-major axis plot can be used to estimate the enclosed mass in an edge-on disk model (see Table 1).

We describe our results for each of these regions in the following sections.

### 3.1   G327.12+0.5

This maser cluster has previously been described at arcsecond resolution by P98 who found it to be slightly offset from, but projected on, an HII region. They found the maser components distributed along a line with a constant velocity gradient and their spectrum shows the classic

Keplerian shape. If we combine the maser emission in individual channels we obtain a spatial distribution matching that of P98.

Our observations (Figure 1) confirm the maser emission distribution of P98, although the flux density has decreased significantly. The peak flux density observed at the ATCA in 1994 was 73.6 Jy; we detect only 28 Jy. We find, however, that the concurrent autocorrelation observations measure nearly the same levels as those contained in our models. Therefore we are confident that source variability is the cause of the difference.

Our spectrum also shows the signature three-peaked profile of a classic Keplerian disk (Figure 2), making this one of the best candidates for the emission to define a disk. We confirm that the emission is from a single cluster, which extends across 690 mas with a RMS scatter of 21 mas from the line of best fit. The equivalent size, at a kinematic distance of 5.5 or 8.8 kpc, is 1900 AU or 3040 AU respectively. If gravitationally bound by a massive central object, this implies an enclosed mass of 17.1 or 27.4 $M_\odot$ . Whilst the overall distribution lies along a straight line a closer inspection of the individual components (see Figure 1a) shows that the velocity structure is neither smooth nor simple. Another point of interest can be seen in the velocity-major axis diagram (Figure 1b) which shows that the emission from individual channels tend to extend perpendicularly from the major axis of the cluster. We therefore confirm that our VLBI observations are consistent with P98, but show that the maser emission doesn't arise in a smooth disk and is very disordered on mas scales.

## 3.2   G327.40+0.4

P98 resolved this region into three separate clusters of emission; G327.402+0.444, G327.402+0.445 and G327.402+0.444E. (Note that in P98 figure 10 the labels for G327.402+0.444 and G327.402+0.445 are swapped.) We too detect maser emission from the same three sites. P98 report G327.402+0.444E has only a single, weak, component, at $-74$ km s$^{-1}$. The other two sites, G327.402+0.444 and G327.402+0.445, have peak velocities of $-82.4$ and $-75.3$ km s$^{-1}$. Using the mean velocity of the strongest maser cluster gives a near kinematic distance of 5.1 kpc and a far distance of 9.2 kpc. We have plotted the relative positions of all the maser emission in Figure 3.

G327.402+0.444 (Figure 4) exhibits a confused morphology, with no clear velocity gradient along the major axis at a position angle of 10°. The velocity range is $-84$ to $-80.5$ km s$^{-1}$, and assuming the source is at the near kinematic distance of 5.1 kpc the linear

size of the maser cluster is 239 AU. G327.402+0.445 is a weaker cluster (peak flux density 230 Jy) with an angular size of 540 mas at a position angle of 72 degrees (Figure 5). In P98 these two clusters are taken as separate sources, which we agree with. They find that these sources both lie projected on an H_{II} region with flux density of 199 mJy/beam. For cluster G327.402+0.444 we did not detect the components labeled A and B in P98, which alters the major axis considerably. The source is known to be highly variable (Caswell et al. 1995). As the axes for G327.402+0.444 and G327.402+0.445 are not aligned the sources are not likely to be directly related and do not seem to form the outer edges of a single body. Furthermore, the enclosed mass for the individual clusters is too small for them to be individual massive star forming regions. The recovered flux density is shown in Figure 6.

### 3.3  G328.24−0.5

This region has been previously imaged by Norris et al. (1993) and P98. Norris et al. (1993) report two sites, separated by 1 arcminute, but overlapping in velocity. P98 report on both centres and describe the Southern one as two "clumps" to the east and west of an H_{II} region and with a velocity separation of almost 10 km s$^{-1}$ . They suggest this morphology and large velocity difference may result from shock fronts, possibly in a bipolar outflow.

We find the same maser emission centres: G328.254−0.532, G328.237−0.548 and G328.237−0.548W. The northern one (G328.254−0.532) was too far from the phase centre to prevent phase wrapping within the integration time on the longest baselines, so images of this cluster are not presented, but the flux densities measured are included in our comparisons with the autocorrelations. This cluster (with velocities between −37 and −39 km s$^{-1}$and also at −50 km s$^{-1}$) has poorer flux density recovery due to the smearing within each integration. Figure 7 shows the imaged maser emission regions and Figure 8 the autocorrelations.

G328.237−0.548 (Figures 9a & b), covering −42 to −47 km s$^{-1}$, is confused and made up of four regions of emission. The peak flux density is 45 Jy at −44.5 km s$^{-1}$ . The angular size of G328.237-0.548 is 300 mas with a position angle is 66°, which corresponds to 460 AU at the near kinematic distance of 3 kpc. The enclosed mass would be 0.4 M$_\odot$. Again the velocity gradient within these spots (where a spot is the emission from within one synthesised beam) does not lie along the major axis, instead lying across it.

G328.237−0.548W, (Figures 9c & d) covering −31 to −37 km s$^{-1}$, is linear and made up of two regions of emission with a position angle of 9°. Using the kinematic distance of

3 kpc the angular extent is 380 mas. The enclosed mass is 2.5 $M_\odot$ and the projected physical extent is 560 AU.

In P98 these two sites are assume to be related, as they lie either side of the peak of an H<small>II</small> region. We find no compelling supporting evidence of this, as neither the position angles of the two sources nor velocity spread within the spots align.

### 3.4   G328.81+0.6

This very widely spaced cluster was observed with the ATCA in 1992 (Norris et al. 1993, 1998). They find the masers to be distributed along a line but with no clear velocity gradient.

We find this region to be made up of two clusters (Figures 10 and 11); G328.809+0.633 and G328.808+0.633, as pointed out by Norris et al. (1993). The region does not display a simple velocity distribution. Our relative positions agree with those published (see Figure 10). The velocity-major axis plot shows no simple overall structure. Again the spread of velocities lies perpendicular to the major axis. At a distance of 3.1 kpc the larger cluster, G328.808+0.633, which covers 1.1 arcseconds, has an extent of 1713 AU. Figure 12 shows the autocorrelations.

### 3.5   G329.03−0.2

This cluster (Figure 13) does not seem to have been observed previously at arcsecond or better resolution. Three clusters form a right angled triangle; G329.029−0.205, G329.029−0.205E, G329.029−0.205S which spans 130 mas. The velocity gradients within these spots do not lie along, but across, the cluster major axis. The near kinematic distance corresponding to the mean velocity is 2.6 kpc, and with an angular extent of 130 mas the physical size is 164 AU.

There is additional weak emission between the velocities of −41 km s$^{-1}$and −50 km s$^{-1}$. The peak position ($\alpha_{J2000} = $ 16:00:30.33 $\delta_{J2000} = $ −53:12:27.4. 13.1, −22.5 arcseconds away from the phase centre) matches the OH maser site G329.03−0.20 (Caswell et al. 1995) and there are three methanol emission regions in the later. As this emission is significantly offset from the phase centre rigorous analysis was not possible, additional observations centred on this region are required for more thorough investigation. Figure 14 shows the autocorrelations.

## 4    DISCUSSION

Norris et al. (1988) found that the 12.2-GHz methanol masers they imaged often appeared to be distributed along a line or curve with some maser sites displaying a monotonic change in velocity along this line. Their observations of the 6.7-GHz methanol transition (Norris et al. 1993) confirmed these findings: 10 of 16 sources had components along a line or arc and half of these linear sources had a velocity gradient along the line. Various instrumental errors that could have created such features have been ruled out (not least by using different techniques) and there are too many sources with this linear geometry for the alignment to have arisen by chance.

There are at least three possible ways a linear distribution of masers could arise in a star forming region; (i) the masers may be embedded in an edge-on, proto-planetary disk around a young star(s), (ii) they may be slung along a collimated outflow or jet from the star(s), or (iii) they may lie along a shock front between regions with different physical conditions.

Bipolar outflows are common in star formation regions (Shepherd & Churchwell 1996). However, such outflows are either broad and uncollimated with low velocities (few km s$^{-1}$) or are well collimated, high-velocity flows. The observed linear geometry implies a high degree of collimation but the line of sight velocity of the methanol masers are offset by at most 5-10 km s$^{-1}$ from the thermal molecular line emission from the same region. Also, the limited proper motion studies that have been undertaken find velocities of only a few kilometers per second (Moscadelli et al. 2002). Norris et al. (1993, 1998) point out that there is no proposed mechanism for producing the high level of collimation implied in linear maser regions and, in any case, the high-energy processes that might produce such jets would probably dissociate the molecules of methanol. Also, the outflow model does not offer any explanation for the uniform gradient seen in some of the linear maser regions. It predicts that the orientation of the line of masers should be radial to the central star or HII region.

Both dense dust (Mueller et al. 2002) and molecular gas (Beckwith & Sargent 1993) are abundant in star forming regions. In particular, the region between the shock and ionization fronts around an HII region may possess conditions conducive to methanol maser emission as has been suggested for OH masers (Elitzur 1992). Thus, the linear geometry observed in maser regions could be the result of these masers tracing the boundary between the differing physical conditions on either side of a smooth shock front. Norris et al. (1993, 1998) argue against this model pointing out that the maser spots do not form a ring around

the (spherically symmetric) HII region and there is no evidence for the existence of smooth and regular shock fronts. Another weakness of this model is that it does not account for the monotonic velocity gradient seen in many sources. Finally, many methanol masers are not associated with detectable HII regions (P98; Walsh et al. 1998).

Star formation models (Lin & Pringle 1990; Hollenbach et al. 1994) frequently invoke disks around young stars. Such disks have indeed been observed in a number of cases (Mundy et al. 1996; Wilner et al. 1996) and are known to be rich in warm molecular gas (Beckwith & Sargent 1993). Thus the conditions for maser emission may well exist. If these disks are observed edge-on a linear distribution of masers would result. Disks seen at a small angle from the edge-on orientation could account for the curved distributions seen in some masers. Norris et al. (1993, 1998) favour this scenario and describe two mechanisms that would account for most of these sources being seen edge-on rather than face-on. They calculate that the column depth required for strong maser radiation can only be achieved in the plane of the disk. Another possibility they point out is that the maser radiation cannot escape in any direction other than the plane of the disk because the disk slices through the surrounding HII region. Any maser emission perpendicular to the disk is likely to be absorbed by the HII region which has been shown (Hollenbach et al. 1994) to be optically thick at centimeter wavelengths. Both these models are illustrated in Figure 12 of Norris et al. (1998). Citing a lack of any difference between their 6.7-GHz and 12.2-GHz data (the 12.2-GHz data should be less affected), they rule out the second model. A final prediction of the disk model is that the masers in a source should lie along a diameter of the HII region with the continuum peak (coincident with the star(s)) near the center of the row of masers.

In support of their disk model Norris et al. (1993, 1998) point out that as a uniformly rotating solid structure a disk would have a uniform velocity gradient. However, the motion is unlikely to be so simple and such a gradient will not always be present. In their sample, about half of the sources with a linear distribution of masers also show a velocity gradient along this line. Such a gradient is difficult to account for in the other two models. A common feature of the velocity-major axis diagrams we have constructed is that the velocity spread in individual maser spots is not along the major axis (the direction of the larger scale velocity gradient) and this is contrary to expectations for a simple models of maser emission in an edge-on disk. The velocity gradient within the spot (where a spot is the emission from within one synthesised beam) is illustrated in Figures 1b, 4b, 5b, 9b, 9d, 11b and 13b. In all cases the velocity spread is not along the major axis.

Modeling the maser sources with linear structure assuming Keplerian motion, Norris et al. (1998) find the velocities and positions of the masers consistent with them being embedded in a rotating disk around a star. Their model also yields disk radii of a few thousands of AU and enclosed masses of a few tens of $M_\odot$ which both agree with theoretical models of disks around massive stars (Lin & Pringle 1990), strongly supporting the disk model. They attribute the absence of the double or triple-peaked spectral profile, characteristic of a Keplerian disk (Ponomarev et al. 1994), to small scale velocity and density perturbations within the disk that reduce the ratio of rotational to turbulent velocity. Finally, they suggest that the methanol regions that are complex i.e. do not show a linear geometry, may result from confusion of two adjacent sources (which higher resolution observations would clarify) or, complex regions may be intrinsically different from linear ones.

P98 discuss a larger sample of 45 sources (of which they have imaged 33 with the ATCA) and report that 17 of them exhibit a linear or curved geometry with 12 of these 17 also displaying a velocity gradient along the line. Of 25 sources they find to be associated with Hii regions, 18 either have their maser components aligned or slightly offset with respect to the peak of the continuum emission. They do not find the reduction in the fraction of linear sources with lower peak flux density that was predicted by Norris et al. (1998). While they find the linear sources consistent with the disk model, they find it difficult to account for sources with complex morphology and suggest the latter arise from different conditions, possibly a shock front.

Using the ATCA to observe an *IRAS*-based sample of 6.7-GHz methanol masers detected at Parkes, Walsh et al. (1998) were able to obtain information on more than 150 regions with arcsecond resolution. Of these, only 97 sources had enough maser spots to allow a meaningful study of their geometry. Sixty one of these sources have no linear structure, 27 have some and only 9 have a well-defined linear structure. Assuming Keplerian motion, they estimate the central mass that will result in the observed radial velocities and find (within the large uncertainties inherent in their methods) that while they cannot rule out the disk model, the derived central mass is often unrealistically high. Walsh et al. (1998) favour the shock hypothesis with the maser spots being dense knots of gas that the passage of the shock has compressed and accelerated. Maser spots require large column lengths with velocity coherence along the line of sight which an near edge-on shock can produce. The velocities observed in the shock model are the projection of the shock velocity onto our line of sight. If the shock is expanding across a homogeneous medium even a smooth velocity

gradient could be produced. This model would result in different maser spot geometries (including lines and curves) depending on local conditions. The shock model does not, in general, produce monotonic velocity gradients and this was a strong argument against it (Norris et al. 1998). Walsh et al. (1998) point out that only 12 of 97 sites in their sample show such a gradient and conclude that a linear velocity gradient is not a regular property of maser sites.

Minier et al. (2000) addressed this issue at VLBI resolution, observing 14 star forming regions at 6.7 and 12.2 GHz using the EVN and VLBA networks, respectively. Ten sources show linear morphology and (mostly) a smooth velocity gradient, in line with the disk model. The sample of Minier et al. includes the remarkable source NGC7538 which contains a long (50 mas) thin continuous region of 6.7- and 12.2-GHz maser emission with a linear velocity gradient (Minier et al. 1998). The velocity gradients observed by Minier et al. (2000) are similar to those measured by P98 and Norris et al. (1998), but the linear extents seen by Minier et al. (2000) are about ten times smaller resulting in sub-solar masses for the putative massive star. Thus higher resolution VLBI images seem to cast doubt on the disk hypothesis though, Minier et al. (2000) suggest they could be only seeing a fraction of the rotating disk, which will underestimate the central mass. The fact that we find the same maser sites as the ATCA observations and recover the majority of the autocorrelation flux density shows that we are not resolving any significant proportion of the disk that is masing on larger scales.

Minier et al. (2002) also compare their zero equivalent flux density to the autocorrelated flux. They find significant shortfall in brightness on the VLBI baselines which they interpret as halos around fully saturated masers. We find some, but much less significant, excess emission in the autocorrelation. This suggests that either the maser spots the we are observing have much less flux density in the halo than the sample of Minier et al. or that our shorter baselines make us more sensitive to the extended emission.

As stated earlier we determined the relative positions of the maser emission features through model fitting the emission in each spectral channel, using the minimum number of model parameters that produced residuals less than five times the RMS noise. Some emission is well modelled with a point source, but much of the emission is resolved or partially resolved. For nearly all the resolved emission a circular Gaussian provides an acceptable fit to the data. Table 2 gives the observed flux density and the size of the circular Gaussian for a representative sample of spots in all sources. The brightness temperatures of the maser emission ranges over 4 orders of magnitude, with the brightest exceeding $10^{12}$ K.

**Table 2.** The spot size of selected maser features. The linear size has been calculated assuming the near kinematic distance in each case.

| Source | Velocity (km s$^{-1}$) | Flux Density (Jy) | Angular size (mas) | Linear size (AU) | Brightness Temperature (K) |
|---|---|---|---|---|---|
| G327.120+0.511 | -83.4 | 1.0 | 6.5 | 36 | $9.4 \times 10^8$ |
|  | -87.1 | 15.0 | 42.0 | 231 | $3.5 \times 10^8$ |
|  | -90.0 | 0.4 | 14.1 | 78 | $8.0 \times 10^7$ |
| G327.402+0.445 | -75.2 | 14.6 | 26.6 | 136 | $8.2 \times 10^8$ |
| G327.402+0.444 | -80.8 | 29.4 | 5.1 | 26 | $4.5 \times 10^{10}$ |
|  | -82.4 | 162.0 | 2.1 | 10 | $1.6 \times 10^{12}$ |
| G328.254−0.532 | -36.2 | 1.9 | 9.9 | 26 | $3.7 \times 10^8$ |
| G328.237−0.548 | -44.6 | 182.0 | 5.6 | 15 | $2.3 \times 10^{11}$ |
| G328.808+0.633 | -44.0 | 50.0 | 35.4 | 110 | $1.6 \times 10^9$ |
|  | -44.5 | 148.0 | 4.8 | 15 | $2.6 \times 10^{11}$ |
| G329.029−0.205 | -37.4 | 112.0 | 4.3 | 11 | $2.4 \times 10^{11}$ |
|  | -40.4 | 4.3 | 6.6 | 17 | $3.9 \times 10^9$ |

The observed linear sizes and brightness temperatures in our sample are similar to those observed by Minier et al. (2002), however, we have been able to satisfactorily model the maser emission with a single component rather than a core/halo structure.

In contrast to the (single-source) VLBI observation reported in Norris et al. (1998) which confirmed the linear geometry revealed by ATCA and the Parkes Tidbinbilla Interferometer data, and suggested ATCA maps were sufficient to determine the broad structure of maser sources, our LBA observations are producing more questions than they answer. There is less sign of a simple linear structure at these resolutions (§3), and the striking feature is the presence of internal velocity gradients perpendicular to the cluster major axis. Calculation of the enclosed mass using the methods of Walsh et al. (1998) yield enclosed masses of only a few M$_\odot$ (see Table 1) casting further doubt on the disk hypothesis. Clearly a new model which more consistently explains the growing wealth of observational information is required.

### 4.1   A new model for linear methanol masers

One of the main arguments that has been put up against the shock model is that the velocity range for the masers is low (in comparison to that observed for water masers) and there have been no suggestions as to how to achieve a highly linear morphology (in many cases with a monotonic velocity gradient) in the absence of highly collimated, high velocity outflows. We will now put forward a model that addresses these objections, inspired by our observations of velocity gradients within individual maser spots which are perpendicular to the major axis of the maser spatial distribution. As has previously been suggested by Walsh et al.

(1998) and others, our model is that class II methanol masers arise behind low-speed ($<$ 10 km s$^{-1}$) planar shocks. This is consistent with the observation that class II methanol masers typically have velocities within 5-10 km s$^{-1}$ of the thermal emission from the same regions and also the proper motion results of Moscadelli et al. (2002), which find velocities in the range 1-7 km s$^{-1}$ for the class II methanol masers in W3(OH). To produce a linear spatial distribution only requires that the shock is propagating nearly perpendicular to the line of sight. Figure 15 illustrates the shock front. Interaction of the shock with density perturbations in the star forming region will gradually disrupt its linearity and reduce it with time. In this model the strongest methanol masers will arise behind shocks that are perpendicular to the line of sight as this is when the path length is greatest. A prediction we can make from this model is that as the inclination angle of the shock increases we would expect a) the peak flux density of the masers to decrease, b) the average linewidth of the masers to increase and c) the internal velocity gradient within a maser spot to increase. This is because as the inclination angle of the shock-front increases, a) the coherence length is reduced, b) a greater range of the star forming region's velocity is sampled and c) the individual channels can be super-resolved along the shock front. The majority of methanol maser sources do not show linear morphologies and these arise in shocks which are seen at angles more highly inclined to the line of sight. For an inclined shock the path length will be shorter and so the chances of having a sufficiently long path with line of sight velocity coherence is decreased. The masers will arise at random locations and show an overall complex morphology. Further, we know that shocks are common in the high-mass cluster mode of star formation and so the presence of linear structures with a small number of offset maser spots can be explained as being due to different shocks. In this case the proper motion of the offset maser features should be systematically different.

An obvious question is why haven't internal velocity gradients perpendicular to the large scale velocity gradient been noticed in previous VLBI observations of methanol masers? There are two possible explanations for this, the first is that many of the sources for which VLBI observations have been made are those with the highest peak flux density. In the model we have proposed the strongest masers are those which are closest to being perpendicular to the line of sight and so those where the effect is smallest. The second possible explanation relates to the way in which maser images are often presented. In many cases, maser emission in consecutive spectral channels which are separated by less than a synthesized beam are represented as a single maser spot at some average position. In doing this any information

on the internal velocity gradient is lost, it is only when data for each individual spectral channel is plotted on a velocity-major axis diagram that the orthogonal orientation of the internal and large scale velocity gradients stands out.

The final remaining question is how to produce a monotonic velocity gradient within a planar shock front. One possibility is that it arises when an edge-on planar shock propagates into a rotating dense molecular clump or star forming core. In general the shock will make some angle to the rotation axis of the clump/core and this will result in a linear gradient in the observed line of sight velocity. This is because the line of sight velocity at the tangential point of the clump is simply $V_{los} = r\omega$ where $r$ is the distance between the shock front and the rotation axis of the clump and $\omega$ is the angular frequency of the clump rotation. This is illustrated in Figure 15. The typical linear dimensions of a methanol maser region are observed to be approximately 0.03 pc (Caswell 1997, P98), while the typical dimensions for cores in high-mass star forming regions is 0.1 pc (Jijina et al. 1999). The dimensions and temperatures of these cores are in the right range to produce methanol masers, although the density and methanol abundance must be orders of magnitude greater in the post-shocked gas than values averaged across the core in order for masing to occur (Cragg et al. 2001, 2002). Moscadelli et al. (2002) have undertaken the only proper motion study of methanol masers and model the observed kinematics as an expanding conical outflow. They propose that the linear feature seen in the 6.7- and 12.2-GHz methanol masers and 6.035-MHz OH masers in W3(OH) arises along one edge of the cone as that produces paths approximately parallel to the line of sight. This is clearly an alternative method of producing linear structures, which is consistent with a shock model for the methanol masers, however, if it were the most prevalent method then we might expect to see X or V like structures in some sources as well, but these have not been observed.

The model we are putting forward to explain our observations, and as a general explanation for the spatial morphologies observed in methanol masers, leads to a number of predictions which enable it to be tested through comparison with observations. Our model predicts the following, with the last two being the most definitive tests.

  (i) The internal velocity gradients within a maser spot should be perpendicular to the major axis of the spatial extension and of a similar magnitude for all spots.

  (ii) The percentage of linear class II sources should be a function of the peak luminosity.

**Table 3.** Maser sites and their parameters. Luminosity is given in Jy kpc$^2$ without any attempt to correct for beaming or distance ambiguities. Line widths are the full detectable velocity range of the central (i.e. brightest) emission group. The final column is the median velocity gradient in each identifiable group and the RMS scatter for that group.

| Source | Distance kpc | Flux Density (Jy) | Luminosity Jy kpc$^2$ | line width km s$^{-1}$ | Velocity gradient range mas/km s$^{-1}$ |
|---|---|---|---|---|---|
| G327.120+0.511 | 5.5/8.8 | 27.5 | 832/2130 | 0.4 | $1 \pm 3$ |
| G327.402+0.444 | 5.1/9.2 | 233 | 6060/19720 | 0.5 | $-3 \pm 4$ |
| G327.402+0.445 | | 18 | 468/1523 | 1.0 | $12 \pm 4$ |
| G328.237−0.548 | 3.0 | 195 | 1760 | 0.7 | $0 \pm 5$ |
| G328.237−0.548W | | 5.5 | 50 | 1.1 | $-1 \pm 5$ |
| G328.808+0.633 | 3.1 | 148 | 1420 | 0.4 | $2 \pm 11$ |
| G329.029−0.205 | 2.6 | 114 | 770 | 1.1 | $0 \pm 4$ |

(iii) The linewidth of the masers should decrease with luminosity and the magnitude of the internal velocity gradient increase.

(iv) The proper motion of the maser spots should be perpendicular to the major axis (compared to being along the major axis for an edge-on disk).

(v) The magnetic field near a shock front should be oriented parallel to the shock and hence parallel to the direction of elongation, while for a disk the magnetic field is expected to thread the disk and hence be perpendicular to the direction of elongation. Polarization observations of the methanol masers should be able to distinguish between these two models, although it may be necessary to go to VLBI resolutions to avoid confusion of the position angle due to multiple maser spots at arcsecond resolutions.

Our sample has only seven well imaged extended sources, but we can investigate whether these match our proposed tests. Tests ii), iv) and v) require further observations, but test i) is fulfilled. For test iii) when we compare the linewidth against luminosity we find the slope is $-0.8 \pm 0.2 \times 10^{-4}$ km s$^{-1}$/Jy kpc$^2$. The outliers are the two narrowest sources, G328.808+0.633, and G327.120+0.511 (see Figure 16a). To estimate the velocity gradients across the source we have grouped those data points close in position (within 5 mas) and velocity, and measured the velocity-major axis gradient. Figure 16b plots the luminosity against the median gradient (in mas/km s$^{-1}$). This shows that the velocity gradients are similar within the clusters, but any correlation with luminocity is hidden by the scatter amongst the sources. A larger sample is required to investigate this proposed relationship properly.

Despite the wide variety of geometries seen in methanol spot distribution in masing regions, the observed size and velocity ranges are relatively narrow suggesting a common mechanism, or at least that there are few astrophysical environments that give rise to class II

methanol masers. VLBI resolution imaging, plausibility arguments relating to the number of sources and other inconsistencies suggest that the disk model is an unlikely scenario to explain the majority of linear methanol maser sources. There exists little support in the literature for the outflow hypothesis and there is growing evidence from observations of $H_2$ that some methanol masers are associated with shocked gas (Lee et al. 2001; De Buizer 2003). Also De Buizer et al. find that the distribution of $H_2$ emission is predominantly parallel with the linear maser structures, which is consistent with our hypothesis, but not with a disk model. The shock hypothesis is consistent with a wide range of geometries that arise from differing local conditions, including linear and curved geometries in a fraction of sources.

## 5   CONCLUSIONS

We have observed five sites of methanol maser emission, and imaged eleven clusters with milliarcsecond resolution. These high resolution images argue strongly that the linear structures commonly observed are more likely linear shock fronts than Keplerian disks and some of the predictions of the former model are fulfilled. We are, however, not able to provide conclusive evidence of this, and VLBI observations of a large sample is required. We have proposed a further series of experiments in which we will collect full polarisation data which should determine the relationships between the maser spots.

**REFERENCES**

Batrla W., Matthews H. E., Menten K. M., Walmsley C. M., 1987, Nature, 326, 49

Beckwith S. V. W., Sargent A. I., 1993, Astrophys. J., 402, 280

Cannon W. H., Baer D., Feil G., Feir B., Newby P., Novikov A., Dewdney P., Carlson B., Petrachenko W. T., Popelar J., Mathieu P., Wietfeldt R. D., 1997, Vistas in Astronomy, 41, 297

Caswell J. L., 1996, Mon. Not. R. astr. Soc., 279, 79

Caswell J. L., Vaile R. A., Forster J. R., 1995, Mon. Not. R. astr. Soc., 277, 210

Churchwell E., Walmsley C. M., Cesaroni R., 1990, Astr. Astrophys. Suppl., 83, 119

Clemens D., 1985, Astrophys. J., 295, 422

Cragg D. M., Sobolev A. M., Ellingsen S. P., Caswell J. L., Godfrey P. D., Salii S. V., Dodson R. G., 2001, Mon. Not. R. astr. Soc., 323, 939

Cragg D. M., Sobolev A. M., Godfrey P. D., 2002, Mon. Not. R. astr. Soc., 331, 521

Darling J., Goldsmith P., Li D., Giovanelli R., 2003, Astr. J., 125, 1177

De Buizer J. M., 2003, Mon. Not. R. astr. Soc., 341, 277

Diamond P. I., 1989, in ASP Conf. Ser. 6: Synthesis Imaging in Radio Astronomy Very Long Baseline Interferometry II: The Techniques of Spectral Line VLBI. pp 379

Dos Santos P. M., Lepine J. R. D., 1979, Nature, 278, 34

Elitzur M., 1992, Astronomical Masers. Kluwer

Ellingsen S. P., von Bibra M. L., McCulloch P. M., Norris R. P., Deshpande A. A., Phillips C. J., 1996, Mon. Not. R. astr. Soc., 280, 378

Forster J. R., Caswell J. L., 1989, Astron. Astrophys., 213, 339

Garay G., Lizano S., 1999, Publs. astr. Soc. Pacif., 111, 1049

Greisen E. W., 1988, AIPS Memo, 61

Hollenbach D., Johnstone D., Lizano S., Shu F., 1994, Astrophys. J., 428, 654

Jijina J., Myers P. C., Adams F. C., 1999, Astrophys. J. Suppl., 125, 161

Lee J.-K., Walsh A. J., Burton M. G., Ashley M. C. B., 2001, Mon. Not. R. astr. Soc., 324, 1102

Lin D. N. C., Pringle J. E., 1990, Astrophys. J., 358, 515

McKee C. F., Tan J. C., 2003, Astrophys. J., 585, 850

Menten K. M., 1991, Astrophys. J. Letters, 380, L75

Menten K. M., Reid M. J., Moran J. M., Wilson T. L., Johnston K. J., Batrla W., 1988, Astrophys. J. Letters, 333, L83

Menten K. M., Reid M. J., Pratap P., Moran J. M., Wilson T. L., 1992, Astrophys. J. Letters, 401, L39

Minier V., Booth R. S., Conway J. E., 1998, Astron. Astrophys., 336, L5

Minier V., Booth R. S., Conway J. E., 2000, Astron. Astrophys., 362, 1093

Minier V., Booth R. S., Conway J. E., 2002, Astron. Astrophys., 383, 614

Minier V., Ellingsen S. P., Norris R. P., Booth R. S., 2003, Astron. Astrophys., 403, 1095

Moscadelli L., Menten K. M., Walmsley C. M., Reid M. J., 1999, Astrophys. J., 519, 244

Moscadelli L., Menten K. M., Walmsley C. M., Reid M. J., 2002, Astrophys. J., 564, 813

Mueller K. E., Shirley Y. L., Evans N. J., Jacobson H. R., 2002, Astrophys. J. Suppl., 143, 469

Mundy L. G., Looney L. W., Erickson W., Grossman A., Welch W. J., Forster J. R., Wright M. C. H., Plambeck R. L., Lugten J., Thornton D. D., 1996, Astrophys. J. Letters, 464, L169

Norris R. P., Byleveld S. E., Diamond P. J., Ellingsen S. P., Ferris R. H., Gough R. G., Kesteven M. J., McCulloch P. M., Phillips C. J., Reynolds J. E., Tzioumis A. K., Takahashi Y., Troup E. R., Wellington K. J., 1998, Astrophys. J., 508, 275

Norris R. P., Caswell J. L., Wellington K. J., McCutcheon W. H., Reynolds J. E., 1988, Nature, 335, 149

Norris R. P., Whiteoak J. B., Caswell J. L., Wieringa M. H., Gough R. G., 1993, Astrophys. J., 412, 222

Ojha R., 2004, in prep.

Phillips C. J., Ellingsen S. P., Rayner D. P., Norris R. P., 1998, Mon. Not. R. astr. Soc., 294, 265

Phillips C. J., Norris R. P., Ellingsen S. P., McCulloch P. M., 1998, Mon. Not. R. astr. Soc., 300, 1131

Plume R., Jaffe D. T., Evans N. J., 1992, Astrophys. J. Suppl., 78, 505

Ponomarev V. O., Smith H. A., Strelnitski V. S., 1994, Astrophys. J., 424, 976

Shepherd D. S., Churchwell E., 1996, Astrophys. J., 472, 225

Shepherd M. C., 1997, in Astronomical Data Analysis Software and Systems VI, A.S.P. Conference Series, Vol. 125, 1997, Gareth Hunt and H. E. Payne, eds., p. 77. Vol. 6, Difmap: an Interactive Program for Synthesis Imaging. p. 77

Szymczak M., Kus A. J., Hrynek G., Kĕpa A., Pazderski E., 2002, Astron. Astrophys., 392, 277

Walsh A. J., Burton M. G., Hyland A. R., Robinson G., 1998, Mon. Not. R. astr. Soc., 301, 640

Walsh A. J., Hyland A. R., Robinson G., Burton M. G., 1997, Mon. Not. R. astr. Soc.,

291, 261

Wilner D. J., Ho P. T. P., Rodriguez L. F., 1996, Astrophys. J. Letters, 470, L117

Wilson W. E., Roberts P. P., Davis E. R., 1995, in King E. A., ed., Proceedings of 4th APT Workshop, Sydney "the LBA correlator". p. 16

Wilson W. J., Barrett A. H., 1972, Astron. Astrophys., 17, 385

Yorke H. W., Sonnhalter C., 2002, Astrophys. J., 569, 846
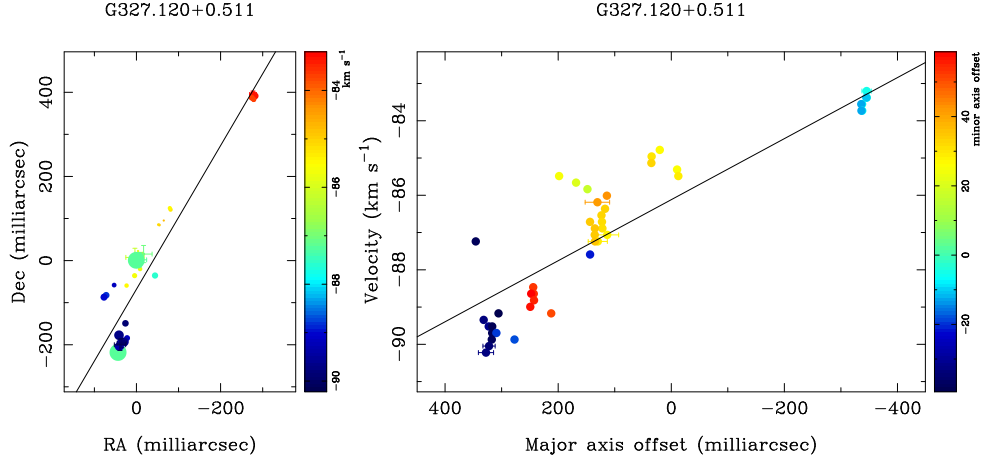
**Figure 1.** a) Maser positions for cluster G327.120+0.511 b) Velocity-Major Axis plot of the same data. In a) we plot the maser emission sites relative to the position reference with the spot sizes proportional to flux density and 1-$\sigma$ error bars. The colours represents the velocity of the spot. The line of best fit shows the proposed major axis of a disk. In b) we show the velocity against the distance along this major axis. The colour represents the distance from this major axis. The line of best fit allows the determination of the enclosed mass.
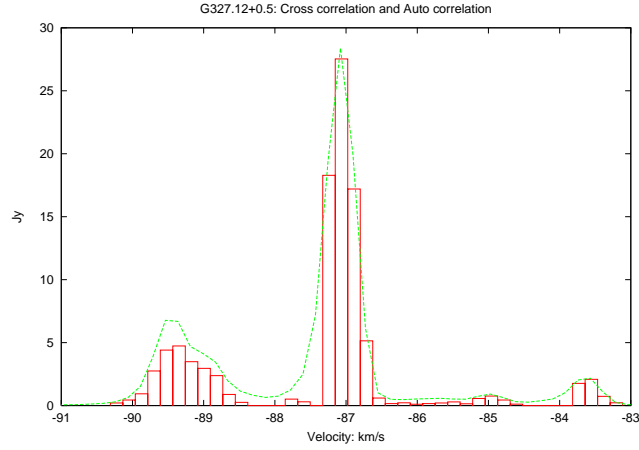


**Figure 2.** Autocorrelation (from Parkes with Antenna temperature subtracted) (dotted line) against equivalent zero spacing flux density (bar graph). This demonstrates the good flux recovery in the model fitting.
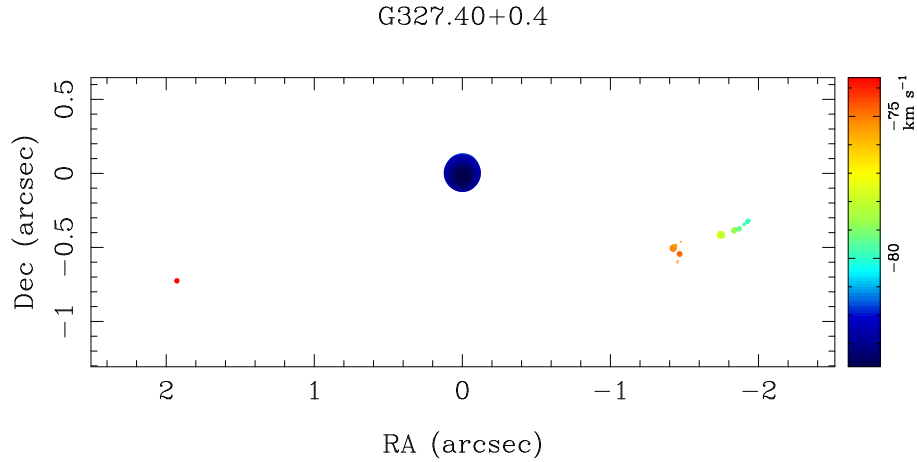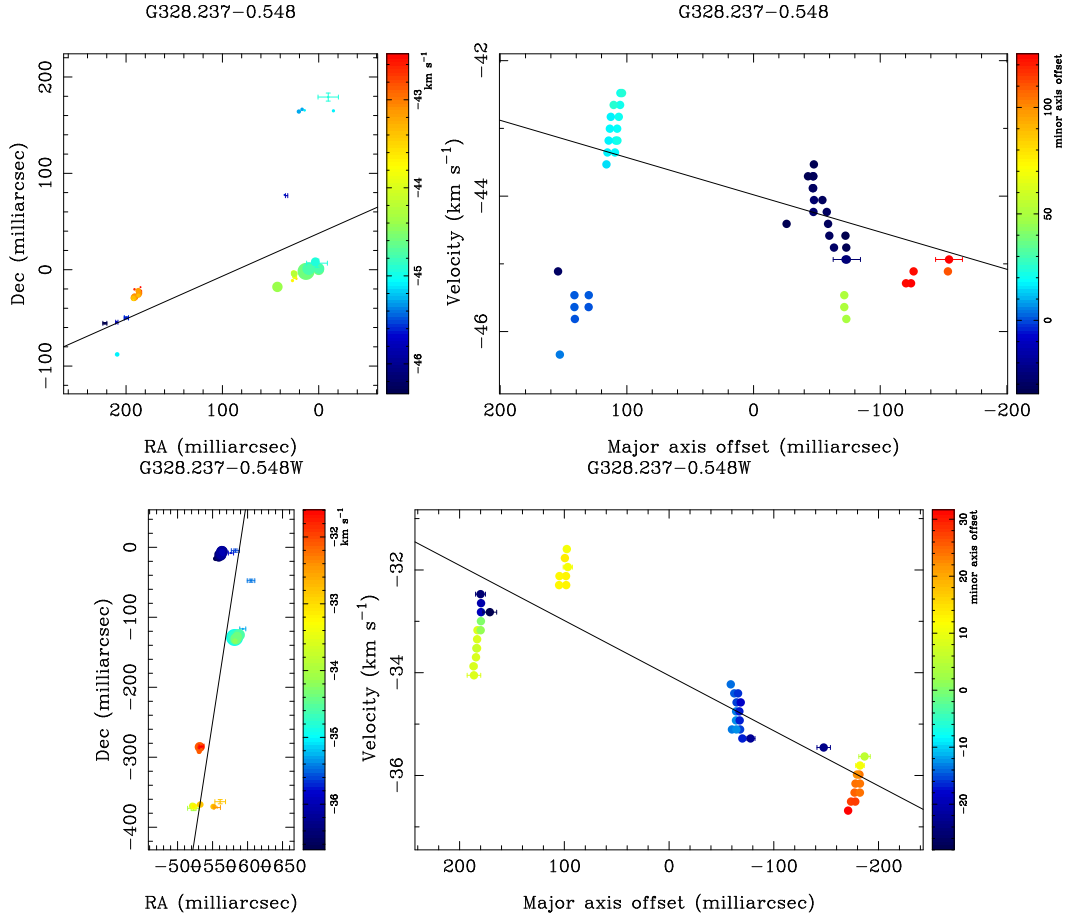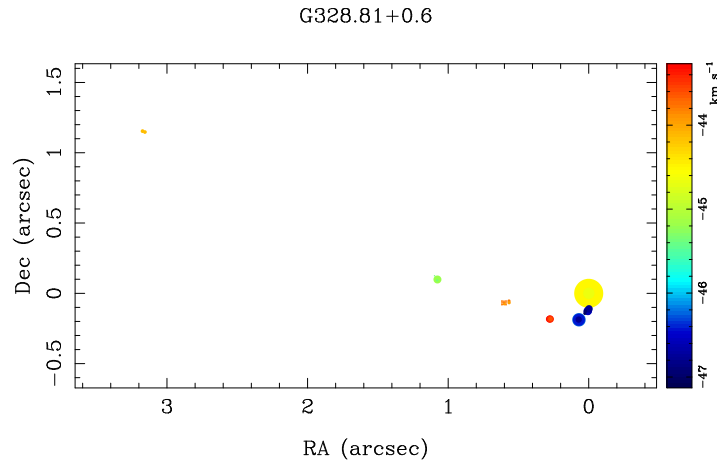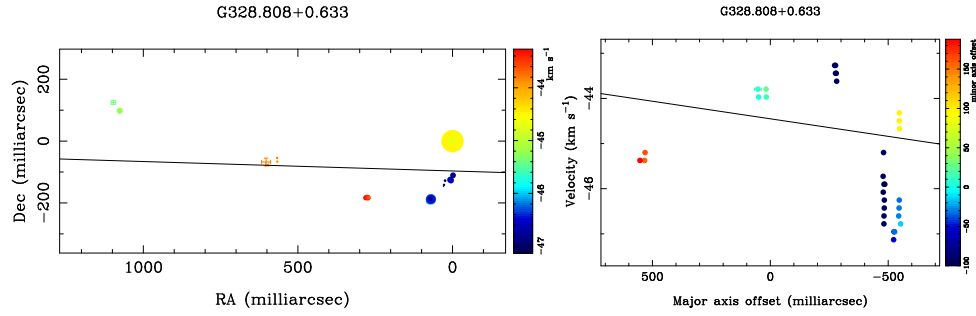


**Figure 3.** Relative maser positions for cluster G327.40+0.44, using the same conventions as Figure 1a
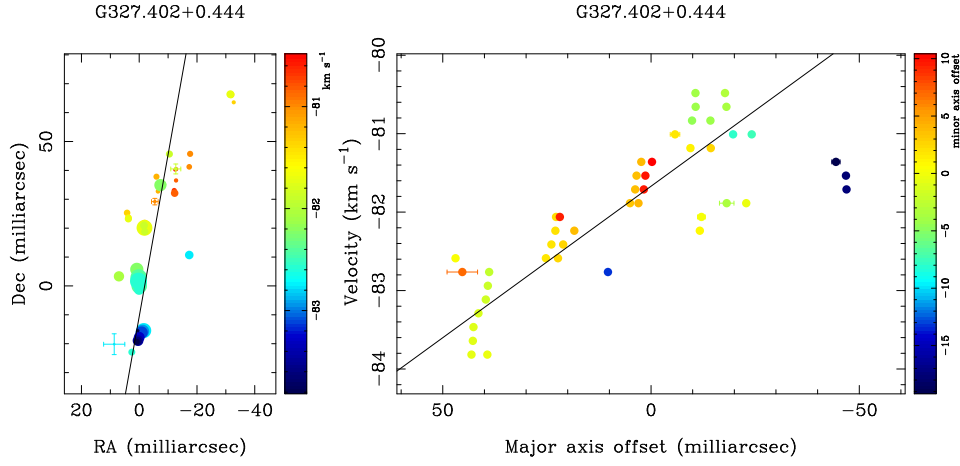
**Figure 4.** a) Maser positions for cluster G327.402+0.444 b) Velocity-Major Axis plot of the same data. These follow the same conventions as Figure 1.
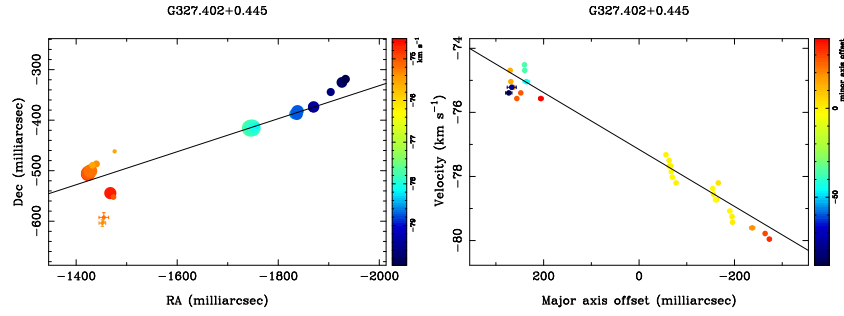


**Figure 5.** a) Maser positions for cluster G327.402+0.445 b) Velocity-Major Axis plot of the same data. These follow the same conventions as Figure 1.
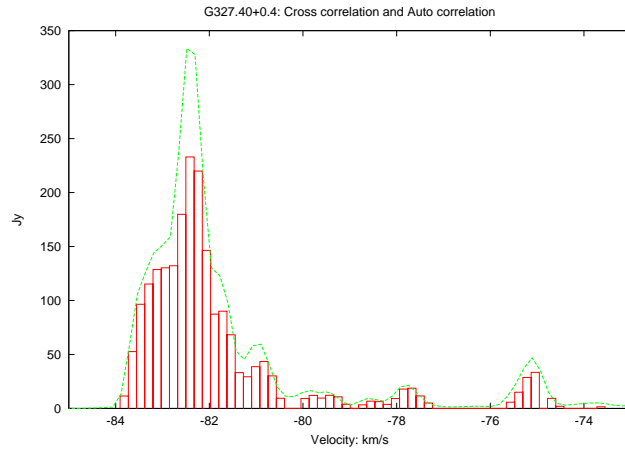


**Figure 6.** Autocorrelation (from Parkes with Antenna temperature subtracted) (dotted line) against equivalent zero spacing flux density (bar graph). This demonstrates the good flux recovery in the model fitting.
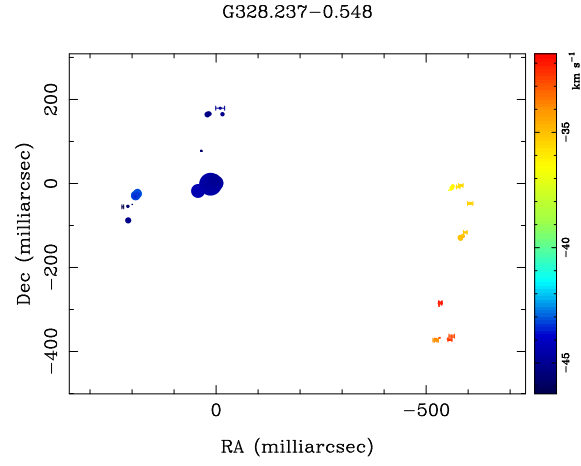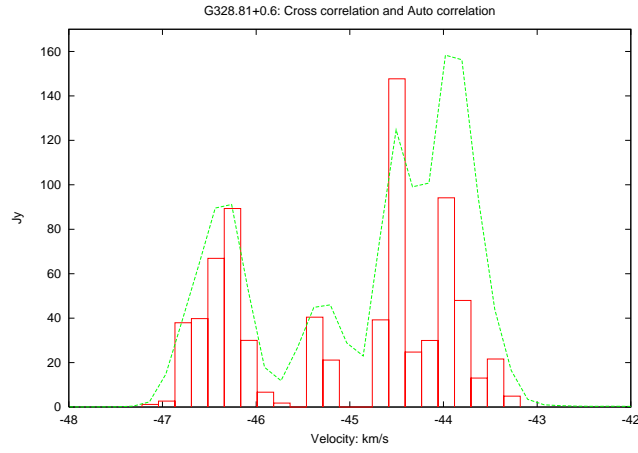
**Figure 7.** Relative maser positions for cluster G328.237−0.548. These follow the same conventions as Figure 1.
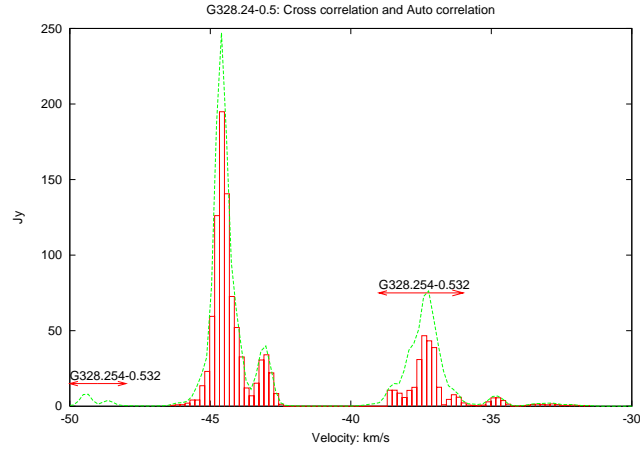


**Figure 8.** Autocorrelation (from Parkes with Antenna temperature subtracted) (dotted line) against equivalent zero spacing flux density (bar graph). This demonstrates the good flux recovery in the model fitting.

**Figure 9.** a) Maser positions for clusters G328.237−0.548, b) Velocity-Major Axis plot of the same data, c) Maser positions for clusters G328.237−0.548W and d) Velocity-Major Axis plot of the same data. These follow the same conventions as Figure 1.
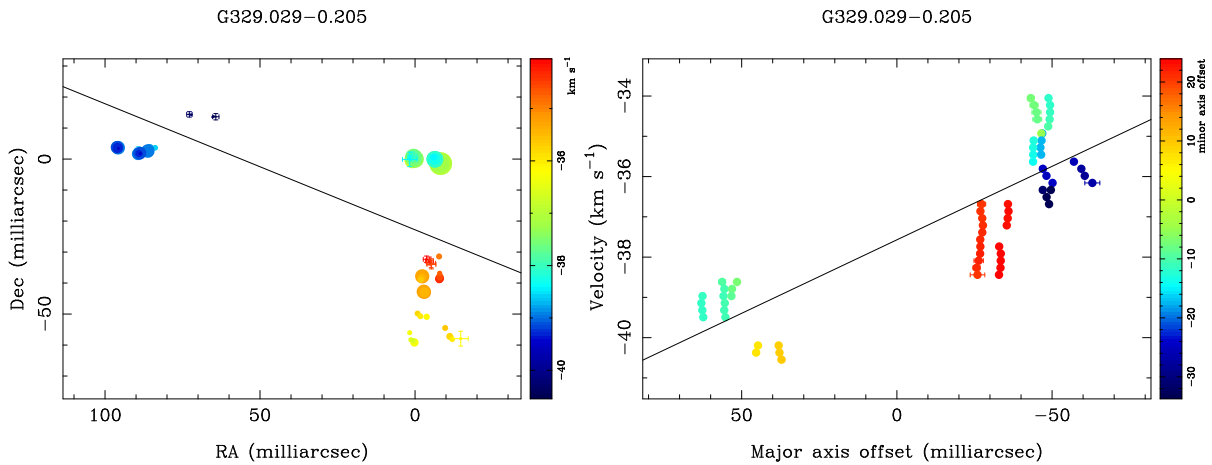


**Figure 10.** Maser positions for clusters G328.809+0.633 and G328.808+0.633. These follow the same conventions as Figure 1a.

**Figure 11.** a) Maser positions for cluster G328.808+0.633 and b) Velocity-Major Axis plot of the same data. These follow the same conventions as Figure 1.



**Figure 12.** Autocorrelation (from Parkes with Antenna temperature subtracted) (dotted line) against equivalent zero spacing flux density (bar graph). This demonstrates the good flux recovery in the model fitting.



**Figure 13.** a) Maser positions for cluster G329.293-0.205 and b) Velocity-Major Axis plot of the same data. These follow the same conventions as Figure 1.
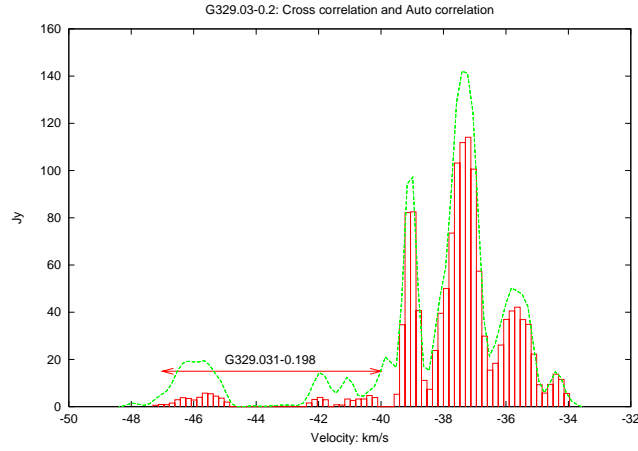
**Figure 14.** Autocorrelation (from Parkes with Antenna temperature subtracted) (dotted line) against equivalent zero spacing flux density (bar graph). This demonstrates the good flux recovery in the model fitting.
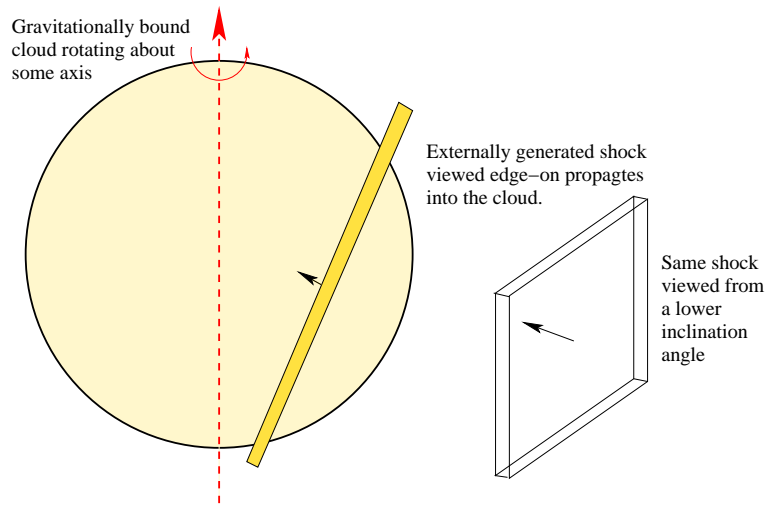


**Figure 15.** Model of the shock and a self-gravitationally bound starforming region.
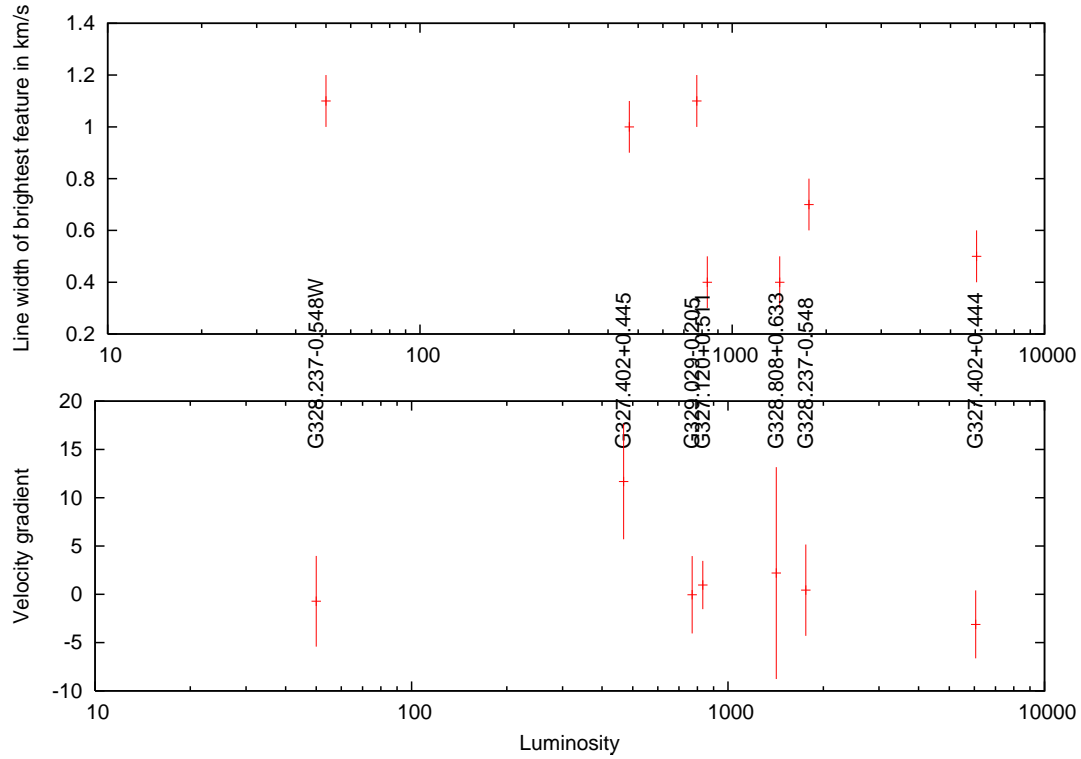
**Figure 16.** The comparison on the model predictions with the data. a) Peak emission line width and b) Median velocity gradients (in mas/km s$^{-1}$) across the sources as a function of luminosity. No estimates of the errors in luminocity have been made, the errors in the linewidths are half the channel width and the errors in the gradients are the RMS of the individual gradients within each cluster.